Diagnosing Plasma Conditions in Targets Irradiated by Intense Light Ion Beams Using K$_\alpha$ Satellite Line Intensity Ratios

J.J. MacFarlane, P. Wang,
J.E. Bailey, T.A. Mehlhorn

June 1997

UWFDM-1047

FUSION TECHNOLOGY INSTITUTE

UNIVERSITY OF WISCONSIN

MADISON WISCONSIN

Diagnosing Plasma Conditions in Targets
Irradiated by Intense Light Ion Beams
Using K_α Satellite Line Intensity Ratios

J. J. MacFarlane,[1] P. Wang,[1] J. E. Bailey,[2] and T. A. Mehlhorn[2]

[1]Fusion Technology Institute
University of Wisconsin-Madison
1500 Engineering Drive
Madison, WI 53706

[2]Sandia National Laboratories
P. O. Box 5800
Albuquerque, NM 87185

Abstract

The characteristics of K_α satellite line emission generated in intense light ion beam experiments are investigated. Inner-shell x-ray lines are emitted from moderate-temperature ($T \sim 10^1 - 10^2$ eV) plasmas as $2p$ electrons of the target ions fill in K-shell vacancies created by beam ion-impact ionization. We focus in particular on the utilization of line intensity ratios from He-like and Li-like ions to diagnose target plasma temperatures and densities. Although the K_α transitions for the He-like and Li-like atomic systems are the same as those in laser-produced and Z-pinch plasmas, the populating mechanisms for their upper states are completely different. That is, the upper states are populated from lower ionization stages by ion-impact ionization. This enables diagnosis of plasmas in the $10 - 100$ eV temperature regime using the extensive instrumentation developed for x-ray crystal spectroscopy. Target plasma characteristics are simulated using a one-dimensional collisional-radiative equilibrium model in which atomic level populations are computed by solving multilevel statistical equilibrium equations self-consistently with the radiation field and ion beam properties. We utilize atomic models which include for all ionization stages a detailed treatment of autoionization states which have K-shell vacancies. Results are presented for Li beam-heated Al and Cl plasmas and proton beam-heated Al plasmas. We find that, as in the case of laser-produced plasmas, the He-like intercombination-to-resonance ratio provides a good density diagnostic. However, because the He_α line is produced in ion beam-heated plasmas with a relatively low degree of ionization, it is less susceptible to resonant self-absorption effects as compared to laser plasmas. In addition, the Li-like satellite line structure is significantly different for plasmas heated by ion beams. Unlike laser-produced plasmas, the Li(dabc) and Li(qr) lines tend to be more intense than the Li(kj) lines. Because of this, we find the Li(dabc)-to-He_α ratio to be a good temperature diagnostic for intense light ion beam experiments. We also discuss the effects of beam-induced multiple ionization, photoionization, and resonant self-absorption on the line ratio diagnostics.

1.   Introduction

X-ray spectroscopy has proven to be a very powerful technique in diagnosing the conditions of high energy density plasmas. For laser-produced and Z-pinch plasmas, where electron temperatures of several hundred eV to more than 1 keV are often attained, K-shell emission spectroscopy utilizing line emission from the H-like and He-like stages of low- to moderate-Z species is commonly used [1–6]. This includes resonance lines as well as satellites which are produced during dielectronic recombination processes [7–9]. In many instances, measuring the intensity ratios of various K-shell lines can provide an accurate determination of the plasma temperature or density. X-ray absorption spectroscopy [10–14] has also been shown to be valuable in diagnosing the conditions in laser-produced plasmas. In some experiments, absorption lines due to inner-shell transitions are utilized to deduce plasma conditions.

Intense light ion beams have been used to generate high energy density plasmas with temperatures of several tens of eV [15–18]. Pulsed power accelerators at Sandia National Laboratories and Forschungszentrum Karlsruhe (FRG) have been used to generate Li and proton beams with power densities of $1-2\,\mathrm{TW/cm^2}$. In these experiments, K-shell electrons from the target ions are ejected due to beam-induced ion-impact ionizations. As the K-shell vacancies are filled by outer shell electrons, K_α ($2p \rightarrow 1s$) lines are emitted on the long wavelength side of the He_α line. As originally pointed out by Nardi and Zinamon [19], K_α satellite lines observed in emission in energetic particle beam experiments can be used to diagnose plasma conditions. For target ions with partially filled L-shells, the wavelengths of the K_α satellites exhibit a detectable shift to shorter wavelengths as the number of L-shell spectator electrons decreases. Thus, the wavelength of the emission reflects the target ionization state. This feature has also been used to investigate hot electron transport in laser-produced plasmas [20,21], where the K-shell vacancies are produced by the energetic electrons. Because of the inner-shell processes which are inherent to light ion beam experiments, x-ray emission spectroscopy can be an effective tool for diagnosing target plasma conditions, even when temperatures are below 100 eV.

The first spectroscopic observation of K_α satellites in intense proton beam experiments was made in Particle Beams Fusion Accelerator II (PBFA-II) experiments at Sandia National Laboratories [15]. More recently, K_α emission spectroscopy has been used to diagnose plasma conditions in PBFA-II Li beam experiments [16,22] and KALIF (Karlsruhe Light Ion Facility) proton beam experiments [18] using planar targets containing thin layers of Al or Mg. In these experiments, time-integrated K_α satellite spectra were recorded using x-ray crystal spectrographs with resolutions of $\lambda/\Delta\lambda \sim 1000-1500$. In

future experiments it is anticipated that tracer dots and time-resolving spectrometers will be used to provide time- and space-dependent diagnostic information about the targets.

In this paper, we investigate the potential of using the ratios of K_α satellite emission line intensities to diagnose temperatures and densities in intense light ion beam experiments. A primary distinction between the beam-induced K_α satellite line emission investigated here and line emission previously studied for laser-produced plasmas is that in this case the upper states of the emitting transitions are populated from lower ionization states via ion-impact ionization (as opposed to dielectronic recombination or electron-impact excitation in laser plasmas). In our study, we have performed collisional-radiative equilibrium (CRE) calculations which not only include a detailed treatment of thermal plasma processes, but also the non-thermal effects of ion-impact ionization of the target K-shell electrons, and detailed modeling of the autoionization states populated by ion-impact processes. Particular attention has been paid to the role of beam-induced multiple ionization (i.e., the simultaneous ejection of more than one target electron during a beam ion-target ion interaction), and resonant self-absorption effects. The goal of the study is to determine temperature-sensitive and density-sensitive line ratios which can be utilized in light ion beam experiments to accurately determine target plasma conditions.

2. Models

In our CRE model, atomic level populations are determined by solving multilevel statistical equilibrium equations self-consistently with the radiation field and ion beam properties. Processes considered in the statistical equilibrium equations include: collisional ionization and recombination; collisional excitation and deexcitation; photoexcitation and photoionization; spontaneous and stimulated emission; radiative and dielectronic recombination; ion beam impact ionization of K-shell and L-shell electrons; and autoionization. In computing the atomic level populations, the photoexcitation rates were computed using a frequency- and angle-averaged escape probability model [23,24]. Photoionization rates were calculated using the mean intensity (i.e., the angle-averaged specific intensity) of the radiation field, which was computed for a grid of frequency points using a multiangle short characteristics model [25]. In computing photoionization rates, only the continuum contribution to the radiation field was considered. That is, the effect of line emission on the photoionization rates was neglected, which is a good approximation because most of the L-shell line emission occurs at photon energies below the L-shell bound-free edges.

2

Our atomic models for Al and Cl each consisted of 500–650 atomic energy levels distributed over all ionization stages. Since the best spectral diagnostic information comes from the relatively high ionization stages — due to the fact that the individual K_α satellite lines are more easily resolved — the N-like through He-like ions were modeled in a greater level of detail. Of the total number of energy levels, roughly 60% were autoionization states with a $1s$ vacancy. A substantial fraction of these had M-shell spectator electrons. This allows for calculating the emission of both K_β ($3p \rightarrow 1s$) lines and K_α lines with M-shell spectators (e.g., $1s^1\, 2s^2\, 2p^5\, 3s \rightarrow 1s^2\, 2s^2\, 2p^4\, 3s$). The latter were observed in proton beam experiments using relatively thick targets [17].

Energy levels and oscillator strengths were calculated using a configuration interaction (CI) model with Hartree-Fock wavefunctions [26]. Relativistic effects were considered in the Breit-Pauli Hamiltonian. The line spectrum is treated in intermediate coupling. Radiative coupling between states is considered for all transitions with oscillator strengths greater than 10^{-5}. Collisional coupling between the levels was "complete" for N-like and higher charge states in the sense that for each ion, all non-autoionizing states were collisionally coupled, as were all autoionizing levels. Coupling between autoionizing and non-autoionizing states includes ion-impact ionization, Auger ionization, and spontaneous decay processes. This level of detail allows one to track transitions into, out of, and between autoionizing states. Electron-impact excitation rate coefficients for resonance and forbidden transitions of N-like and higher charge states were computed using a distorted wave model, while other excitation transitions and electron-impact ionization rate coefficients were obtained using Coulomb-Born and semi-classical impact parameter models.

Autoionization states are populated primarily due to beam ion-impact ionization. The beams are considered to be either fully stripped Li ions or protons. In our model, single ionization (the ejection of a K-shell electron) and multiple ionization (the ejection of a K-shell and one or more L-shell electrons) processes are considered. The ion-impact ionization rate is given by:

$$R_{ii^*} = n_i\, J_B\, \sigma_{ii^*}\left(E_B\right),$$

where J_B and E_B are the beam current density and kinetic energy per ion, $\sigma_{ii^*}(E_B)$ is the ion-impact ionization cross section, and n_i is the number density of target ions in energy level i. The indices i and i^* refer to the initial state and autoionizing state, respectively. Beam ion-impact excitation rates were not included as their rates are insignificant for the target plasma conditions considered in this paper.

Multiple ionization processes tend to be of greater importance for more highly charged beams [27]. Previous studies indicate that multiple ionization does play a role in affecting K_α satellite emission spectra in PBFA-II Li beam experiments [28,22]. To illustrate this, consider the case of the formation of a Be-like K_α satellite. The same line could form due to the following three processes:

$$
\begin{aligned}
1s^2 2s^2 2p^1 & \xrightarrow{KL_0} \\
1s^2 2s^2 2p^2 & \xrightarrow{KL_1} \quad \Big> \quad 1s^1 2s^2 2p^1 \xrightarrow{K_\alpha \text{ emission}} 1s^2 2s^2 , \\
1s^2 2s^2 2p^3 & \xrightarrow{KL_2}
\end{aligned}
$$
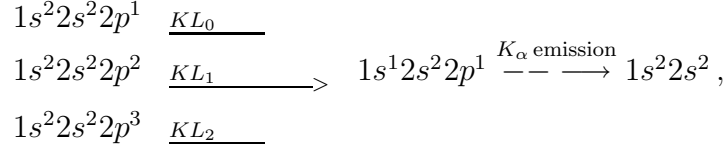
where KL_n refers to the simultaneous ejection of one K-shell and n L-shell electrons from a target ion during its encounter with a beam ion. Thus, a single line can, in principle, originate from several different ionization stages in the bulk plasma.

Ion-impact ionization cross sections are computed [28] using a modified plane-wave Born approximation (PWBA) model in conjunction with an independent probabilistic model based on an effective interaction radius. Corrections to the PWBA model include Coulomb deflection, perturbations on the target ion wavefunctions induced by the projectile, and relativistic effects on the target ion wavefunctions. Figure 1 shows calculated single (KL_0) and double (KL_1) ionization cross sections for Li^{+3} projectiles on three ionization stages of Cl: Cl^{+0}, Cl^{+9}, and Cl^{+13}. The initial state of the target ion was taken to be the ground state; the sole exception to this is $1s - 2p$ double ionization of Be-like Cl, where $1s^2\, 2s^1\, 2p^1$ was the initial state (i.e., the lowest energy configuration with a $2p$ electron). Note that as the ionization state of the plasma increases, the ratio of double to single ionization decreases. This occurs both because the L-shell electrons are more tightly bound in the higher ionization stages and because there are less L-shell electrons.

Despite the relatively low double ionization cross sections for the more highly charged target ions, multiple ionization can still affect the observed K_α satellite emission spectrum. This is because the emission which escapes the plasma often comes from the most highly charged ions in the ionization distribution (as discussed in Section 3). As an example, the He_α line can be produced by both

$$
1s^2\, 2s^1 2p^1 \xrightarrow{KL_1} 1s^1\, 2p^1 \xrightarrow{He_\alpha} 1s^2
$$

and

$$
1s^2\, 2p^1 \xrightarrow{KL_0} 1s^1\, 2p^1 \xrightarrow{He_\alpha} 1s^2
$$
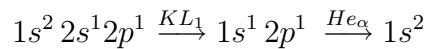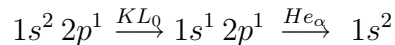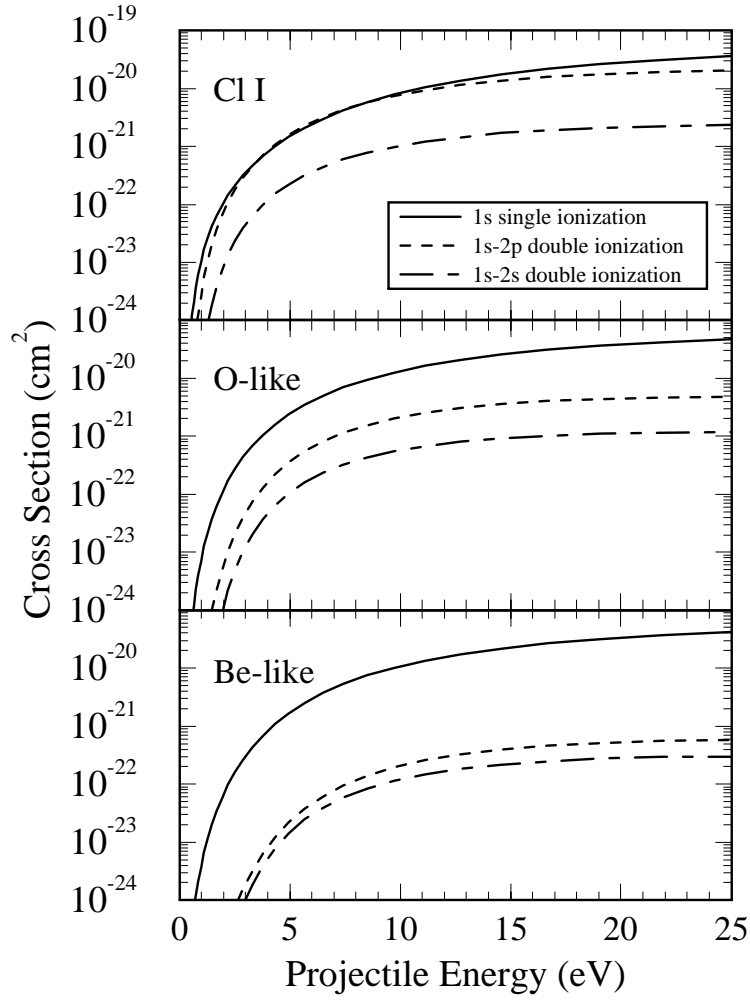
Figure 1. Ion-impact ionization cross sections computed for Cl^{+0} (neutral), Cl^{+9} (O-like), and Cl^{+13} (Be-like) chlorine irradiated by Li^{+3} projectiles. The cross sections for the ionization of a single K-shell electron (solid curves) are compared with those for double ionization (the simultaneous ejection of one K-shell and one L-shell electron).

reactions. Since the rate of each reaction is proportional to the population of its initial state, the lower double ionization cross section can be compensated for by the higher Be-like ionization fraction.

In addition to ion-impact ionization, K_α emission line intensities are also dependent on the fluorescence yield. Fluorescence yields and Auger rates were calculated for each autoionization level using an L-S coupling formalism with Hartree-Fock wavefunctions. The calculated fluorescence yields have been benchmarked with previously published results for Al and Ne [29,30], and agreement was typically found to be better than 10%. The rate at which K_α photons are emitted is:

$$R_{i^* j} = n_{i^*} A_{i^* j},$$

where $A_{i^* j}$ is the spontaneous decay rate and the subscript j refers to the lower state index. The Auger rate can be expressed as:

$$R_{i^* \kappa} = [Y_{i^*}^{-1} - 1] \, n_{i^*} \sum_j A_{i^* j},$$

where Y_{i^*} is the fluorescence yield of autoionizing state i^*, and index κ refers to the ground state of the next higher ionization stage. Table 1 lists our calculated wavelengths, spontaneous emission, and autoionization rates, Γ, for selected He-like and Li-like transitions of Al and Cl. A corresponding energy level diagram is shown in Figure 2.

After the atomic level populations are obtained, line intensity ratios are obtained using an escape probability model. In this way, the populations and emergent line fluxes are computed in a consistent way; i.e., using the same resonant self-absorption model. Results for emission spectra were computed by solving the radiative transfer equation along a line-of-sight perpendicular to the target surface. The source function and opacities include all sources of bound-bound, free-free, and bound-free (including inner-shell) transitions. Voigt profiles are assumed for the lines. Line widths include contributions from natural, Auger, Doppler, and Stark broadening.

3. Results

We next present spectral and line ratio results for light ion beam-heated plasmas, using beam and plasma parameters typical of those in light ion fusion experiments. Unless otherwise noted, we consider the cases of monoenergetic 10 MeV Li^{3+} beams and 5 MeV proton beams. Results are shown for thin target (or tracer) plasmas composed of either

6

Table 1. He-like and Li-like K$_\alpha$ Satellite Transition Data

Name*	Transition	Aluminum			Chlorine		
		λ (Å)	$A(s^{-1})$	$\Gamma(s^{-1})$	λ (Å)	$A(s^{-1})$	$\Gamma(s^{-1})$
α	$1s^2\ ^1S_0 - 1s\,2p\ ^1P_1$	7.757	2.91(13)	0	4.443	8.92(13)	0
IC	$1s^2\ ^1S_0 - 1s\,2p\ ^3P_1$	7.806	6.01(10)	0	4.467	8.25(11)	0
n	$1s^2\,2p\ ^2P_{1/2} - 1s\,2p^2\ ^2S_{1/2}$	7.795	3.29(12)	5.45(13)	4.457	7.86(12)	6.44(13)
m	$1s^2\,2p\ ^2P_{3/2} - 1s\,2p^2\ ^2S_{1/2}$	7.799	8.86(12)	5.45(13)	4.461	3.09(13)	6.44(13)
s	$1s^2\,2s\ ^2S_{1/2} - 1s\,2s\,(^3P)\,2p\ ^2P_{3/2}$	7.805	2.42(12)	7.81(13)	4.463	5.97(12)	9.60(13)
t	$1s^2\,2s\ ^2S_{1/2} - 1s\,2s\,(^3P)\,2p\ ^2P_{1/2}$	7.806	3.67(12)	7.48(13)	4.464	1.52(13)	8.70(13)
q	$1s^2\,2s\ ^2S_{1/2} - 1s\,2s\,(^1P)\,2p\ ^2P_{3/2}$	7.846	2.48(13)	5.31(12)	4.481	7.93(13)	4.20(12)
r	$1s^2\,2s\ ^2S_{1/2} - 1s\,2s\,(^1P)\,2p\ ^2P_{1/2}$	7.848	2.36(13)	8.62(12)	4.483	7.02(13)	1.33(13)
a	$1s^2\,2p\ ^2P_{3/2} - 1s\,2p^2\ ^2P_{3/2}$	7.857	3.47(13)	2.23(12)	4.486	1.11(14)	8.59(12)
b	$1s^2\,2p\ ^2P_{1/2} - 1s\,2p^2\ ^2P_{3/2}$	7.853	4.65(12)	2.23(12)	4.482	9.84(12)	8.59(12)
c	$1s^2\,2p\ ^2P_{3/2} - 1s\,2p^2\ ^2P_{1/2}$	7.860	1.25(13)	2.47(11)	4.490	3.66(13)	1.26(12)
d	$1s^2\,2p\ ^2P_{1/2} - 1s\,2p^2\ ^2P_{1/2}$	7.857	2.72(13)	2.47(11)	4.486	8.82(13)	1.26(12)
k	$1s^2\,2p\ ^2P_{1/2} - 1s\,2p^2\ ^2D_{3/2}$	7.876	1.29(13)	1.26(14)	4.493	4.57(13)	1.45(14)
j	$1s^2\,2p\ ^2P_{3/2} - 1s\,2p^2\ ^2D_{5/2}$	7.875	1.31(13)	1.28(14)	4.496	4.11(13)	1.53(14)

Exponents in parentheses.

*Satellite line names based on Refs. [3] and [7].

1s 2p —— $^1P_1$

—— $^3P_1$

1s 2p^2 —— $^2S_{1/2}$

1s 2p^2 —— $^2P_{3/2}$
—— $^2P_{1/2}$

—— $^2D_{5/2}$

1s 2p^2 —— $^2D_{3/2}$

$^2P_{3/2}$
1s2s(^{3}P)2p ——
—— $^2P_{1/2}$

$^2P_{3/2}$
1s2s(^{1}P)2p ——
—— $^2P_{1/2}$

He$_\alpha$ He IC

a   b

c   d

k   j

m   n

s   t

q   r

1s^2 —— $^1S_0$

1s^2 2p —— $^2P_{3/2}$
—— $^2P_{1/2}$

1s^2 2s —— $^2S_{1/2}$
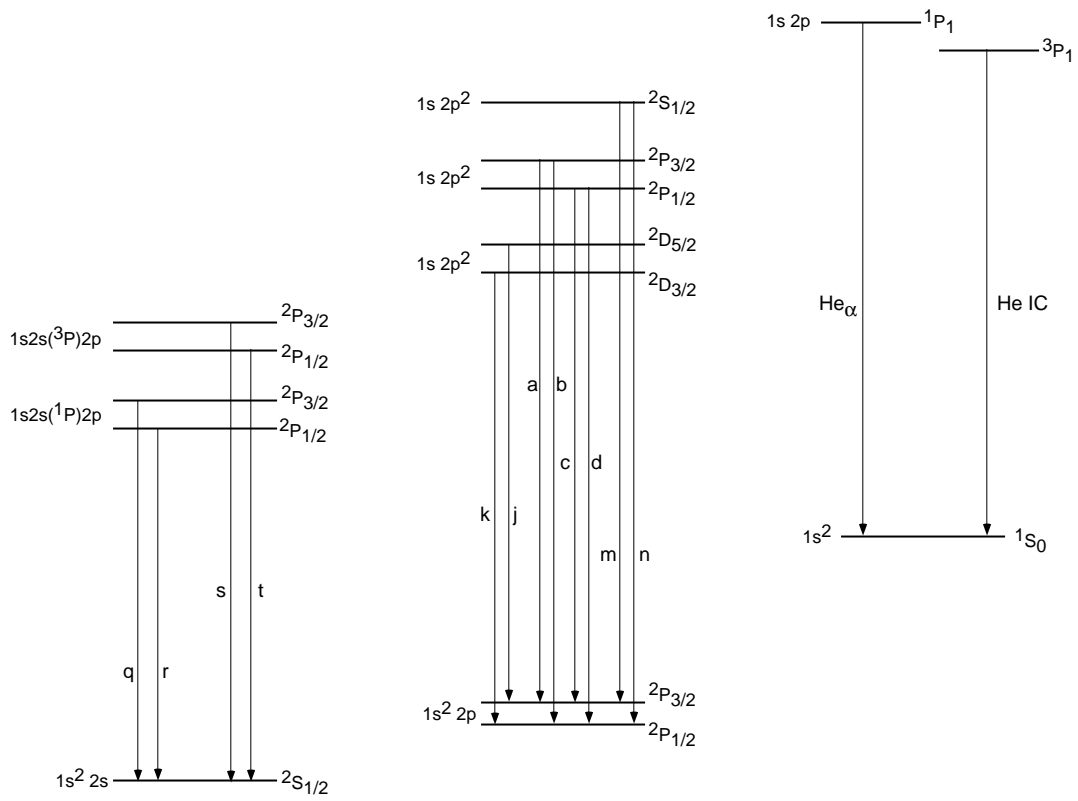
Figure 2.   Schematic energy level diagram showing selected Li-like and He-like transitions.

Al or Cl. The total areal mass for the Al is 54 μg/cm^2 (corresponding to a solid density thickness of 2000 Å), while that for the Cl was 71 μg/cm^2. In all calculations, the target plasmas are assumed to have spatially uniform temperature and density distributions.

Results are shown for temperature and density ranges relevant to light ion fusion experiments. While the temperatures are typically much lower than those attained in laser-plasma experiments, significant line emission from He- and Li-like ions can be readily observed because the upper states of the K$_\alpha$ states are populated from *lower* ionization stages (by beam-impact ionization) as opposed to being populated from higher ionization stages (e.g., by dielectronic recombination) which occurs in laser-produced plasmas.

Figure 3 shows calculated K$_\alpha$ satellite emission (top) and absorption (bottom) spectra for a Cl plasma irradiated by a 10 MeV Li beam. Plasma temperatures range from $T = 80$ eV to 110 eV. In each case the Cl ion density was 6×10^{19} ions/cm^3. Figure 4 shows in more detail the emission spectrum from a $T = 100$ eV, $n = 3 \times 10^{19}$ ions/cm^3 calculation with the He-like lines and Li-like satellites identified. For the absorption spectra shown in Figure 3, the transmission ($e^{-\tau_\nu}$) is computed along a path perpendicular to the planar plasma. Since the absorption strength of a line depends on the population of the lower state of the transition, the transmission spectra reflect the ionization distribution of the plasma. Thus, at $T = 80$ eV Be-, B-, C-, and N-like Cl are the dominant ionization stages. The peak emission at $T = 80$ eV is due to Li-, Be- and B-like Cl. The fact that higher ionization stages are seen in emission is due to two effects. First, for these plasma conditions the emission lines are the result of ion-impact ionization processes in which either one (KL_0) or two (KL_1) electrons are ejected. Note, however, that the apparent "shift" of *two* ionization stages between absorption and emission results not from ion-impact double ionization (KL_1) processes, but rather due to opacity effects. That is, in calculations where resonant self-absorption effects were neglected, the B-like and C-like K$_\alpha$ satellites produce significantly more emission than the Li-like satellites for the same plasma conditions.

Note in Figure 4 that the strongest Li-like satellites are the Li(qr) and Li(dabc) lines, while the Li(kj) lines are relatively weak. The opposite is true for the case of laser-produced plasmas, where the Li(kj) lines tend to be relatively strong. This occurs because in laser-produced plasmas the upper states of the Li-like satellites are populated by dielectronic recombination (whose rate is proportional to the autoionization rate), while in ion beam-heated plasmas the K$_\alpha$ upper states are populated by ion-impact ionization. A simple 3-level atom analysis indicates that for a laser plasma the line intensity is proportional to:

9
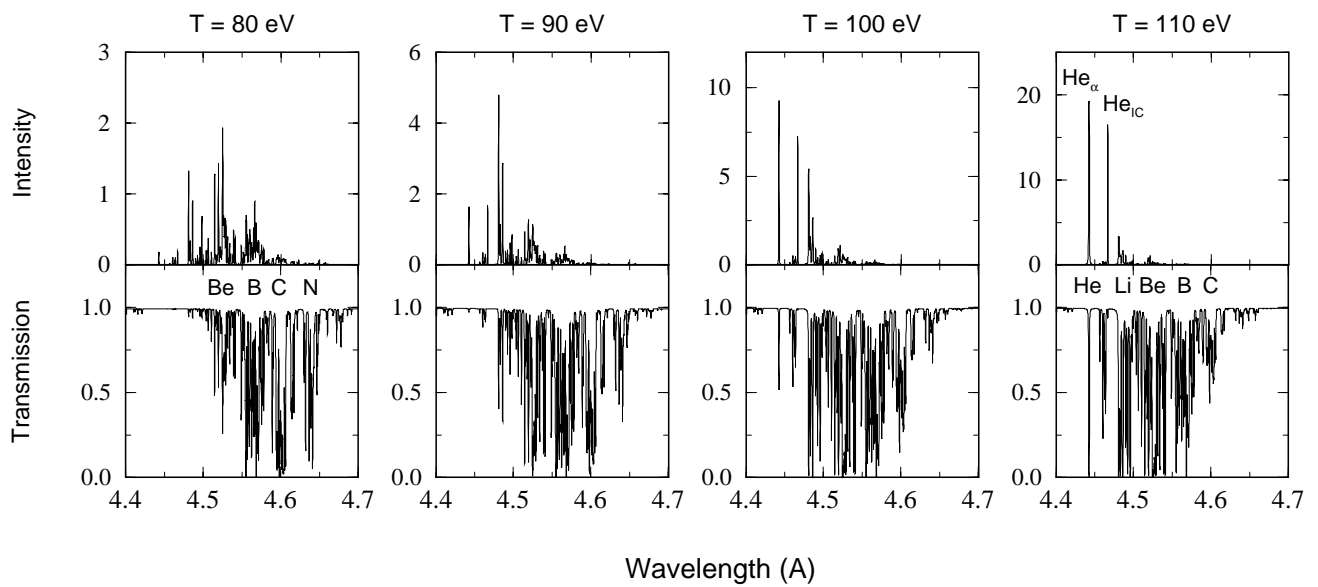
Figure 3. K_α satellite emission and absorption spectra calculated for a Cl plasma irradiated by a 10 MeV Li beam. In each case the Cl ion density is 6×10^{19} ions/cm^3 and the thickness is 0.2 mm. K_α satellite wavelengths for various Cl ionization stages are shown in the lower left and lower right plots.

10
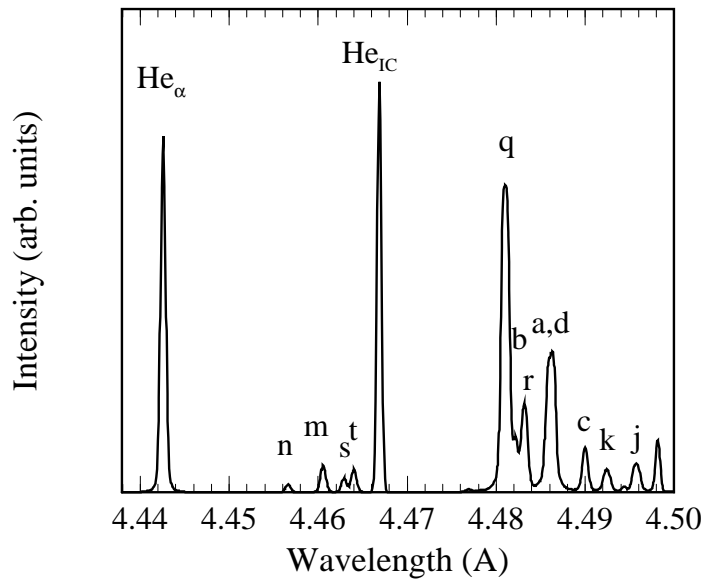
Figure 4. K_α satellite emission spectrum calculated for a Cl plasma irradiated by a 10 MeV Li beam. The Cl temperature is 100 eV, the ion density is 3×10^{19} ions/cm^3, and the plasma thickness is 0.4 mm. The labelled lines correspond to the transitions shown in Figure 2.

$$I_L \sim A_{ul}\Gamma/(A_{ul} + \Gamma) \quad .$$

On the other hand, for ion beam-heated plasmas the line intensity is proportional to:

$$I_L \sim A_{ul}\sigma_{ii^*}/(A_{ul} + \Gamma) \quad ,$$

where σ_{ii^*}, Γ, and A_{ul} are defined as in Section 2. Note that the values of Γ (see Table 1) for the Li(kj) lines are significantly higher than for the other satellites. Because of this the Li(kj) lines observed in laser experiments tend to be fairly prominent, whereas in light ion beam experiments they are relatively weak.

Figure 3 also shows that the optical depth of the He$_\alpha$ line (λ = 4.443 Å) is $\lesssim$ 1 until temperatures exceed 100 eV. Due to the fact that the He-like excited states are populated by ion-impact ionization, the He$_\alpha$ line can have sufficient intensity to be readily observed while at the same time having a small optical depth. Because of this, the He intercombination-to-resonance ratio (discussed below) tends to be much less susceptible to resonant self-absorption — which can cause uncertainties in determing plasma densities — than in the case of laser-produced plasmas.

As the temperature increases from T = 80 eV to 110 eV, the Li-like and He-like lines become strongest in emission. Note that the intensity scale changes in these plots, and that the intensities of the He- and Li-like lines are significantly higher than those of the lower ionization stages. This results from the fact that the fluorescence yields for the lower ionization stages are relatively low (in fact, the fluorescence yields for the He-like lines are unity because their upper levels are not autoionizing states). Note also that for the densities shown ($n_{\rm ion} = 6 \times 10^{19}$ ions/cm^3; $n_e = 6.3 - 7.3 \times 10^{20}$ cm^{-3}) the He intercombination line ($1s\,2p\,^3{\rm P}_1 - 1s^2\,^1{\rm S}_0$) is predicted to be approximately as intense as the He$_\alpha$ line. In addition to being relatively intense, the K$_\alpha$ lines of He-like and Li-like ions are good candidates for diagnosing plasma conditions based on line ratios because their line structure and atomic physics is less complex than the relatively low ionization stages.

Figure 5 shows line ratios for Li(dac)/He$_\alpha$ and Li(qr+b)/He$_\alpha$ as a function of temperature for Li-heated Cl at ion densities ranging from 10^{19} to 10^{21} ions/cm^3. For chlorine, the Li(b) satellite is grouped with the Li(qr) satellite because their line positions are very close (see Table 1; see also Ref. [3]). The Li/He$_\alpha$ line intensity ratios are predicted to decrease by factors of $\sim 30 - 100$ over this density range as the Cl plasma temperature increases from T = 70 eV to 120 eV. This simply results from the fact that the mean ionization state changes from roughly N-like Cl to Li-like Cl over this temperature range. It is also seen in Figure 5 that for the densities shown, the Li/He$_\alpha$ intensity ratios are not
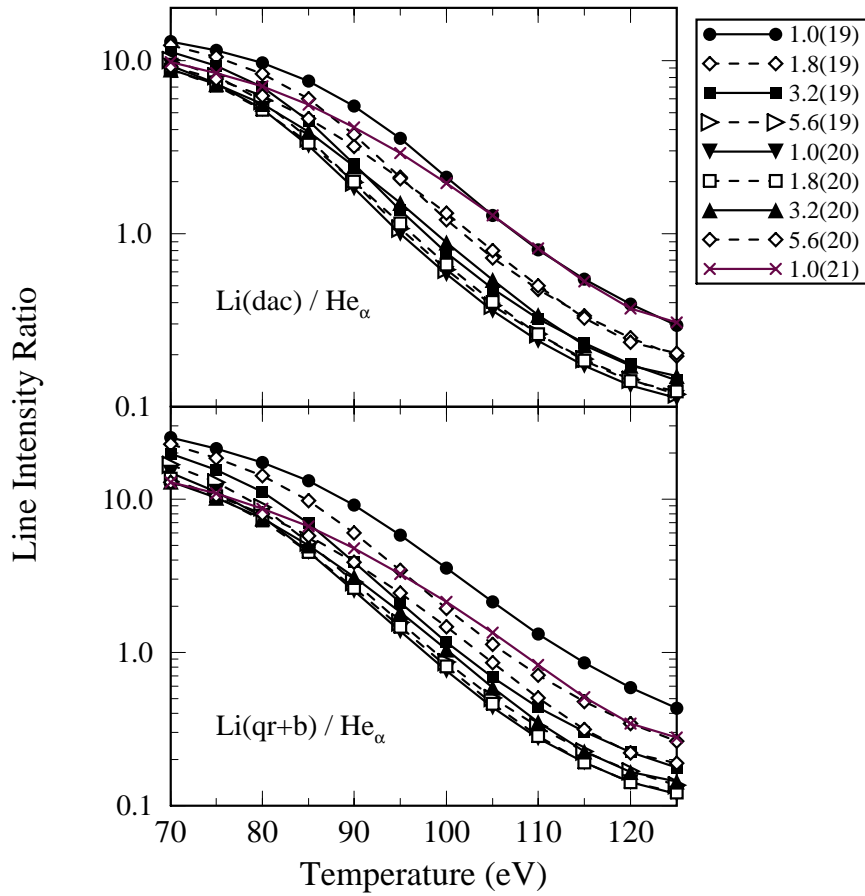
Figure 5. Li(dac)/He$_\alpha$ and Li(qr+b)/He$_\alpha$ line intensity ratios vs. temperature for a Cl plasma irradiated by a 10 MeV Li beam. Each curve represents a fixed ion density. The Cl ion column density ($= n_i \Delta L$) is 1.2×10^{18} ions/cm^2 in all cases.

13

an exceptionally strong function of the density. For instance, if the measured $Li(dac)/He_\alpha$ intensity were ≈ 1, the predicted temperature would be between 96 and 110 eV, so long as the density was between 10^{19} and 10^{21} ions/cm^3.

Figure 6 shows the He_{IC}/He_α line intensity ratio as a function of density. As in the case of higher temperature laser-produced plasmas [31–33], the He intercombination-to-resonance ratio is predicted to be a good density diagnostic. This again results from the fact that at relatively low densities the $1s\,2p\,^3P_1$ state (i.e., the upper state of the He_{IC} transition) does not collisionally depopulate in an effective manner. In this case, its intensity is affected more by the rate at which it is being populated, as opposed to its oscillator strength. At high densities, collisions push the population distribution more toward LTE (i.e., a Boltzmann distribution), and the low oscillator strength of the intercombination line leads to weak emission.

As pointed out in previous studies [3,8], the nearly coincident wavelengths of the He_{IC} and $Li(st)$ lines can potentially lead to problems in the interpretation of experimental data. The calculated separation of the chlorine Li-like s and t satellites of chlorine relative to the He_{IC} line is 4 and 3 mÅ, respectively. By comparison, the calculated separations listed in Ref. [3] are 1.3 and 0.2 mÅ. The intrinsic line widths of the He_{IC} and $Li(st)$ lines are $\sim 0.5 - 0.7$ mÅ over the range of plasma conditions considered here. These lines tend to be dominated by Doppler broadening, with the $Li(st)$ affected marginally by Auger decay. In cases where there is an intrinsic overlap of lines, photoexcitation and absorption of one line by another must be considered. For Cl, our calculations predict this is not the case. Nevertheless, in many circumstances the instrumental spectral resolution may not be sufficient to resolve the He_{IC} and $Li(st)$ features. The bottom plot in Figure 6 shows the intensity ratio for the sum of the He_{IC} plus $Li(st)$ lines relative to He_α. For $T \gtrsim 100$ eV this ratio also shows little dependence on temperature, thus making it a very good density diagnostic. At $T \lesssim 90$ eV, the contribution from the $Li(st)$ doublet becomes high enough to show a pronounced temperature sensitivity.

A similar set of results is shown in Figures 7 and 8 for the case of an Al plasma irradiated by a 10 MeV Li beam. In Figure 7, it is seen that the $Li(dabc)$ satellite-to-He_α ratio is found to be a good temperature diagnostic for Al plasmas at $T \sim 30 - 60$ eV and ion densities $\sim 10^{18} - 10^{20}$ ions/cm^3. However, at higher densities the $Li(dabc)/He_\alpha$ and $Li(qr)/He_\alpha$ ratios show a somewhat greater density sensitivity. (For Al, the $Li(b)$ was grouped with $Li(dac)$ because of their similar wavelengths.) Figure 8 shows the He_{IC}/He_α and $(He_{IC} + Li(st))/He_\alpha$ ratios as a function of density. Again, the He IC-to-resonance ratio is seen to be a good density diagnostic, exhibiting little temperature sensitivity. The
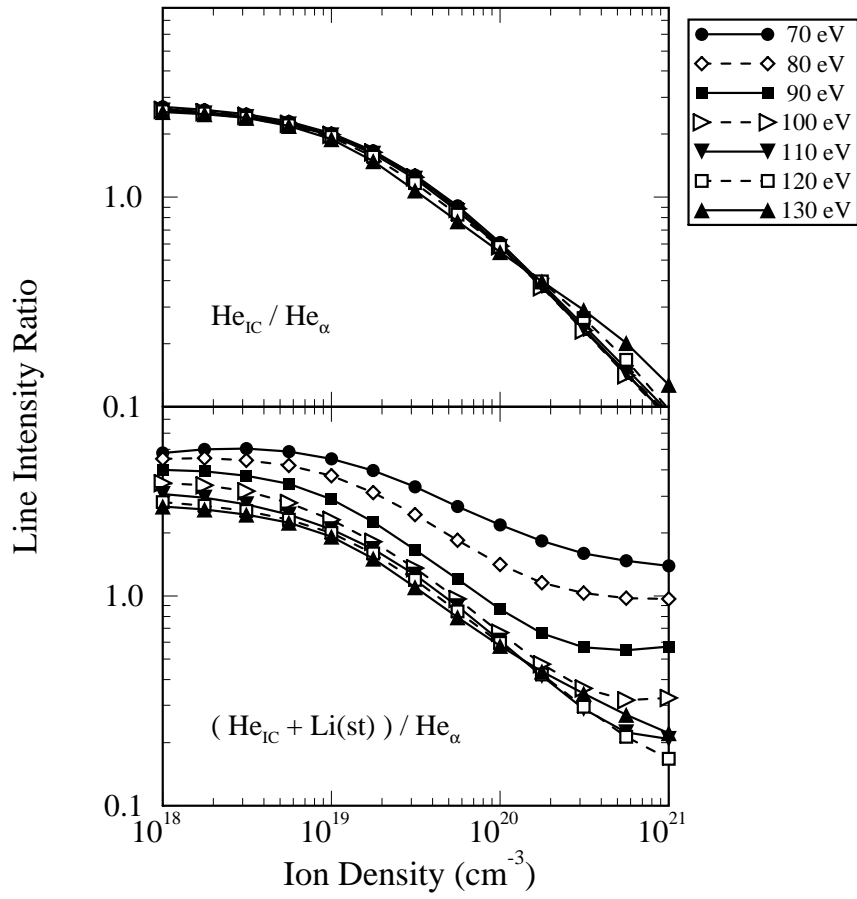
Figure 6. He_{IC}/He_{α} and $[He_{IC} + Li\,(st)]/He_{\alpha}$ line intensity ratios vs. ion density for a Cl plasma irradiated by a 10 MeV Li beam. Each curve represents a fixed temperature. The Cl ion column density is 1.2×10^{18} ions/cm^2 in all cases.

15
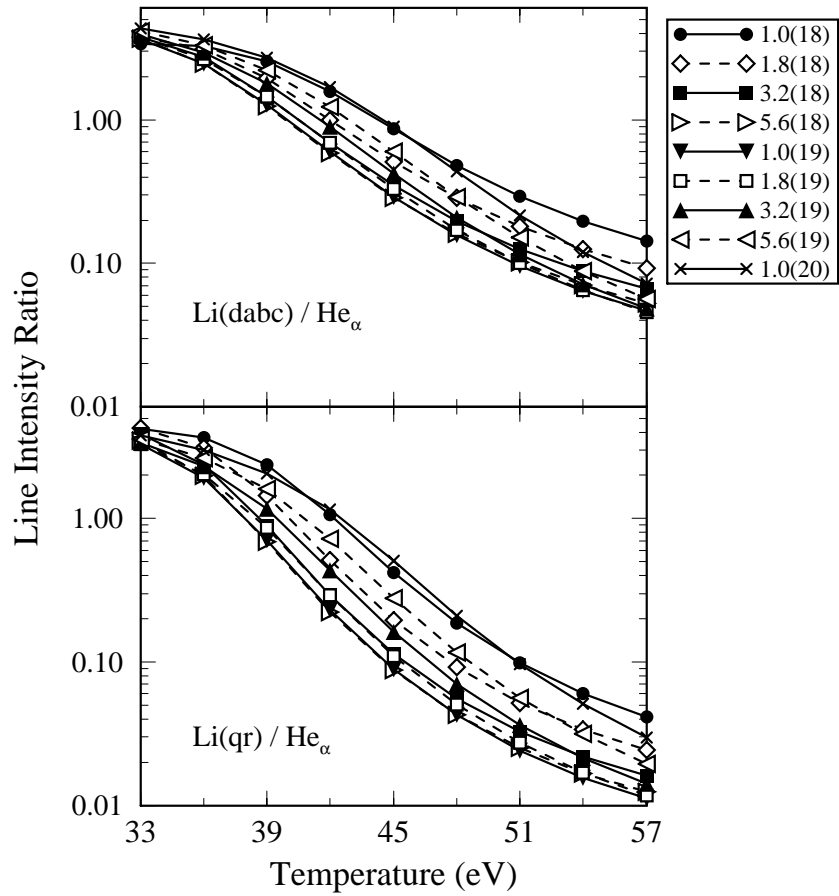
Figure 7. Li (dabc)/He$_\alpha$ and Li (qr)/He$_\alpha$ line intensity ratios vs. temperature for an Al plasma irradiated by a 10 MeV Li beam. The Al ion column density is 1.2×10^{18} ions/cm^2 in all cases.
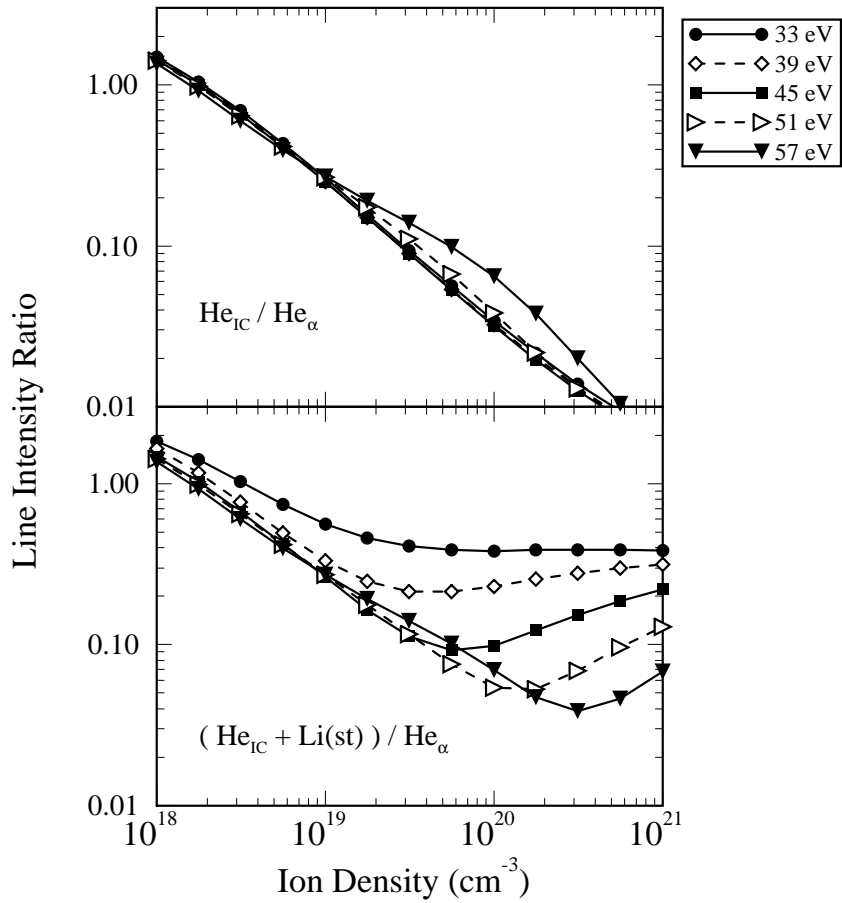
Figure 8. He_{IC}/He_α and $[He_{IC} + Li\ (st)]/He_\alpha$ line intensity ratios vs. ion density for an Al plasma irradiated by a 10 MeV Li beam. The Al ion column density is 1.2×10^{18} ions/cm^2 in all cases.

17

nearby Li(st) satellites are seen to impact this ratio at relatively high densities and low temperatures; that is, at lower plasma ionization states.

We next examine the effects of opacity and beam-induced multiple ionization processes on line ratios. In the case of multiple ionization, it is important to assess the significance of this process because the multiple ionization cross sections are considered to be more uncertain than single ionization (one K- no L-shell ejections) cross sections. This uncertainty stems from the lack of experimental data for multiple ionization in ionized plasmas.

Figure 9 compares temperature-dependent line ratios from our baseline simulations (which includes beam-induced multiple ionization) to those from simulations in which multiple ionization (i.e., KL_n, where $n \geq 1$) was neglected. Results are shown for the Li(acd)/He$_\alpha$ ratio of Cl and the Li(dabc)/He$_\alpha$ ratio of Al. (Results are very similar for the Cl Li(qr+b)/He$_\alpha$ and Al Li(qr)/He$_\alpha$ ratios.) In each case the ion density was 3×10^{19} ions/cm^3. It is seen that at this density multiple ionization significantly alters the line intensity ratios at $T \lesssim 90$ eV for Cl and $T \lesssim 42$ eV for Al. The reason for this can be readily understood by examining the plasma ionization distribution. Figure 10 (top plot) shows that at $T = 80$ eV, the Li-like ionization fraction — from which He$_\alpha$ forms via a single ionization process — is approximately 10^{-3}, while the Be-like ionization fraction is 0.046; i.e., about a factor of 60 higher. This is comparable to the ratio of the single-ionization to double-ionization cross section for highly ionized Cl (see Figure 1). Thus, at relatively low temperatures the lower double ionization cross section can be more than compensated for by the ratio of ionization fractions. At relatively high temperatures, the ionization fractions become comparable and beam-induced single ionization becomes the dominant populating mechanism.

Figure 11 shows the fractional populating and depopulating rates for $1s\,2p\,^1{\rm P}_1$ (upper state of He$_\alpha$) and $1s\,2s\,(^1{\rm P})\,2p\,^2{\rm P}_{3/2}$ (upper state of the Li(q) line). Each fractional populating rate is defined by the rate at which the level is populated by a given process divided by the total populating rate. The dominant populating rates are beam-induced single and multiple ionization, electron-impact collisional excitation and deexcitation from other He-like $1s\,2\ell$ or Li-like $1s\,2\ell\,2\ell'$ states, and photoexcitation due to resonance self-absorption processes. The dominant depopulating rates are K$_\alpha$ fluorescence, autoionization (in the case of Li-like satellites), and collisional excitation/deexcitation to other $1s\,2\ell$ and $1s\,2\ell\,2\ell'$ states. Figure 11 shows that for the $1s\,2p\,^1{\rm P}_1$ state the beam-impact single ionization rate exceeds the multiple ionization rate at $T \gtrsim 85$ eV. A similar situation occurs for the upper state of Li(q) for $T \gtrsim 75$ eV. Our calculations indicate that a significant
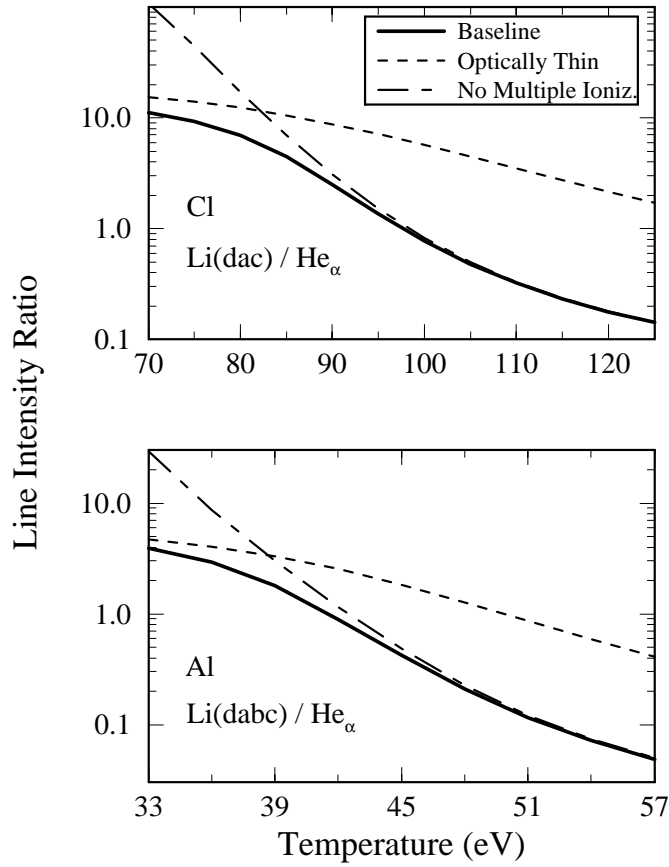
Figure 9. Dependence of temperature-sensitive Li/He$_\alpha$ line intensity ratios on ion-impact multiple ionization and opacity effects. Top plot: chlorine Li(dac)/He$_\alpha$; bottom plot: aluminum Li (dabc)/He$_\alpha$. The parameters for the baseline simulations are identical to calculations discussed previously with $n = 3 \times 10^{19}$ ions/cm^3.
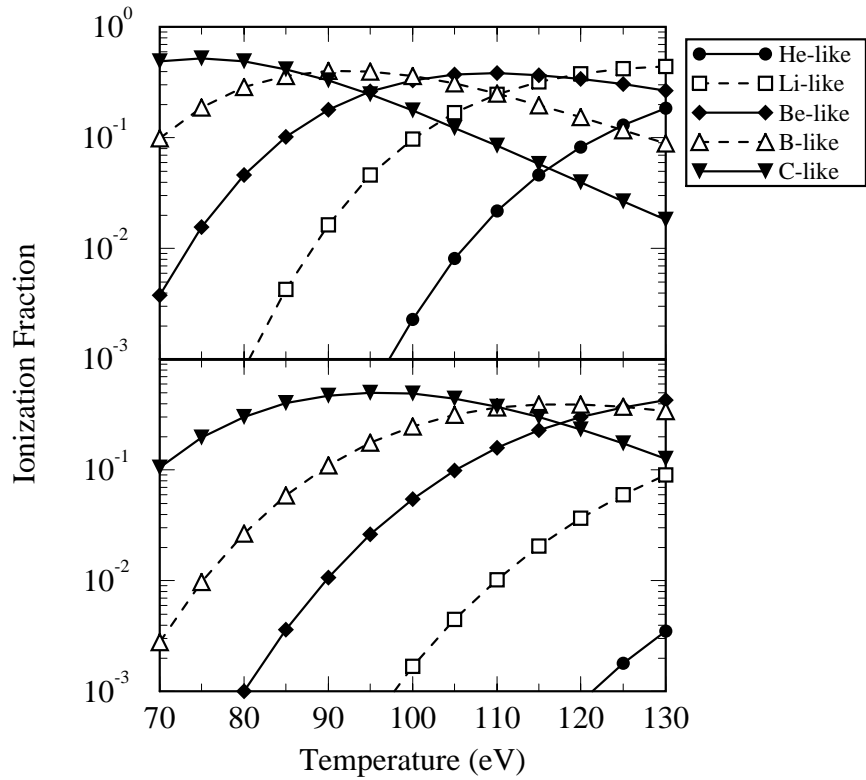
Figure 10. Ionization fractions calculated for $n = 3 \times 10^{19}$ ions/cm^3 Cl plasmas. Top plot: baseline calculations with Cl ion column density of 1.2×10^{18} cm^{-2}; bottom plot: optically thin case.
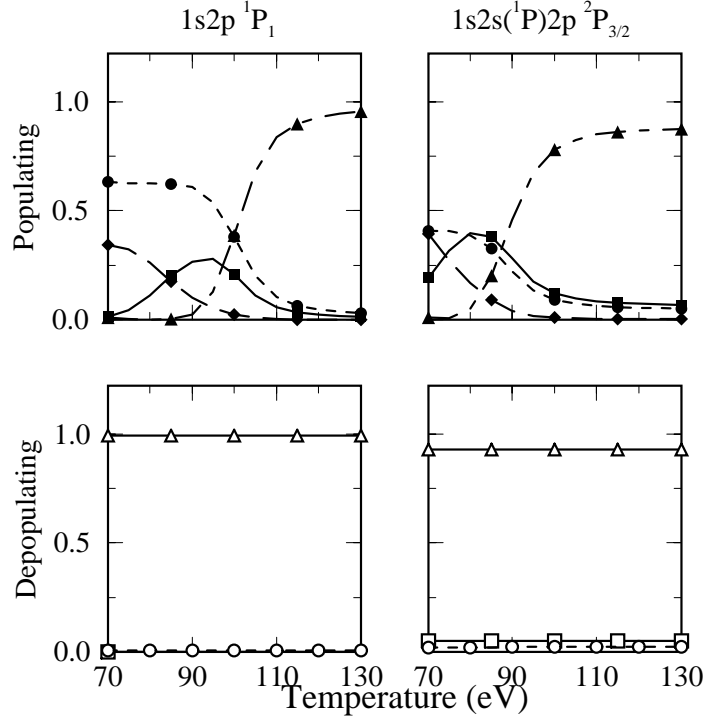
Figure 11. Fractional populating and depopulating rates for the $1s\,2p\ ^1\mathrm{P}_1$ and $1s\,2s\,(^1\mathrm{P})\,2p\ ^2\mathrm{P}_{3/2}$ states of a Cl plasma with $n = 3 \times 10^{19}$ ions/cm^3 as a function of temperature. Populating rates shown are: filled triangles: photoexcitation from the $1s^2\ ^1\mathrm{S}_0$ and $1s^2\,2s\ ^2\mathrm{S}_{1/2}$ states (i.e., their K$_\alpha$ transitions); filled circles: collisional excitation/deexcitation from other $1s\,2\ell$ and $1s\,2\ell\,2\ell'$ states; filled squares: ion-impact single (KL_0) ionizations; filled diamonds: ion-impact multiple (KL_n, $n \geq 1$) ionizations. Depopulating rates are: open triangles: K$_\alpha$ fluorescence; open squares: autoionization; open circles: collisional excitation/deexcitation to other $1s\,2\ell$ and $1s\,2\ell\,2\ell'$ levels.

21

component of the He$_\alpha$ line emission results from beam-induced populating of $1s\,2p\,^3$P and $1s\,2s$ states, which then populates the $1s\,2p\,^1$P$_1$ state by electron-impact excitations (filled circles). For the $1s\,2s\,(^1$P$)\,2p\,^2$P$_{3/2}$ state (as well as some of the other doublet autoionizing levels), a significant source of population results from collisional coupling with the quartet autoionizing states. At relatively high temperatures, photoexcitations due to resonant self-absorption becomes the dominant populating mechanism, while spontaneous emission is the dominant depopulating mechanism. Thus, at high temperatures "scattering" of the K$_\alpha$ line radiation tends to become important.

Figure 12 shows the density dependence of the fractional population rates of the $1s\,2p\,^1$P$_1$ and $1s\,2p\,^3$P$_1$ (upper state of the He$_{\rm IC}$ transition). The $1s\,2p\,^3$P$_1$ state is seen to be primarily populated by collisional excitations and deexcitations from $1s\,2\ell$ states (filled circles); in particular, other $1s\,2p\,^3$P and $1s\,2s\,^3$S states. At low densities, it tends to be depopulated by emission of a photon. As the density increases, collisional coupling between the singlet and triplet states increases, resulting in the well-known density dependence of the He$_{\rm IC}$/He$_\alpha$ ratio. The relative importance of collisional couplings with other $1s\,2\ell$ levels is also seen in the populating rates for the $1s\,2p\,^1$P$_1$ state. It is also seen that over the entire density range studied, this state is primarily depopulated by the emission of a He$_\alpha$ photon.

Figure 9 also compares results from our baseline case with those from a series of optically thin plasma calculations. Here, it is seen that opacity effects significantly lower the predicted Li/He$_\alpha$ ratios by factors of a few. One might suspect this would be in part due to the fact that the Li-like satellites achieve line center optical depths $\sim 10^0 - 10^1$ at temperatures $\gtrsim 100$ eV, as shown in Figure 13. At $T \lesssim 120$ eV, the He$_\alpha$ line center optical depth tends to be lower than that of the strongest Li-like lines. However, the major reason for the relative increase in the He$_\alpha$ line intensity with increasing optical depth is the change in the ionization distribution caused by photoexcitation and photoionization. Figure 10 compares the ionization distributions from optically thin and optically thick calculations. Since the intensity of the Li and He lines is simply a reflection of the ionization fractions of Be and Li — neglecting for the moment multiple ionization — let us examine the Be/Li ionization ratio. At $T = 100$ eV and $n = 3 \times 10^{19}$ ions/cm^3, the ionization ratio of Be/Li is 32 in the optically thin case, while it is 3.4 in the optically thick case. Thus, the lower Li(dac)/He$_\alpha$ ratio in the optically thick case stems from opacity-induced changes to the ionization distribution. When photoionization is ignored, but photoexcitation is included, the Be/Li ionization ratio is 4.4, which is still a factor of 7 lower than the optically thin case. Thus, we conclude that photoexcitation followed by collisional ionization, as well as
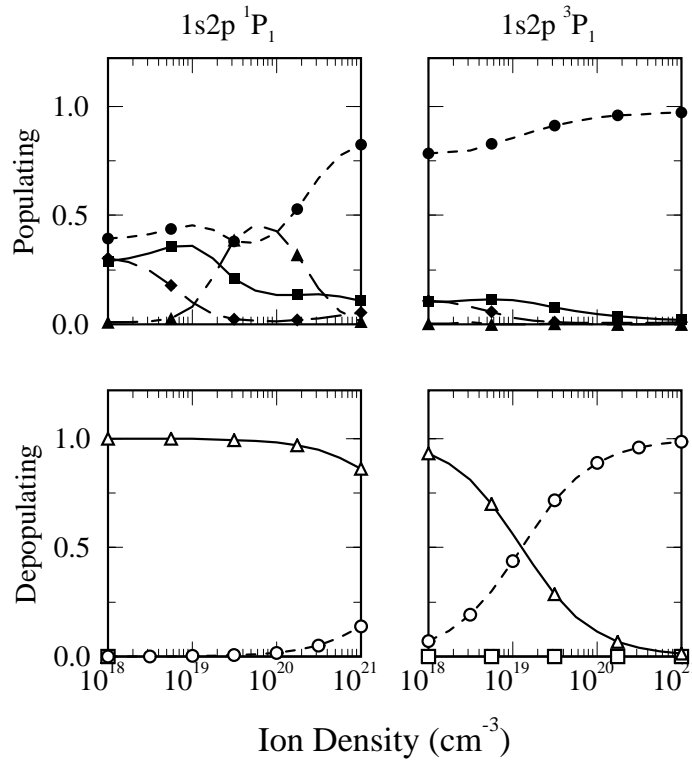
Figure 12. Fractional populating and depopulating rates for the $1s\,2p\,^1P_1$ and $1s\,2p\,^3P_1$ states of a Cl plasma with $T = 100$ eV as a function of ion density. Symbol definitions are identical to those in Figure 11.

23
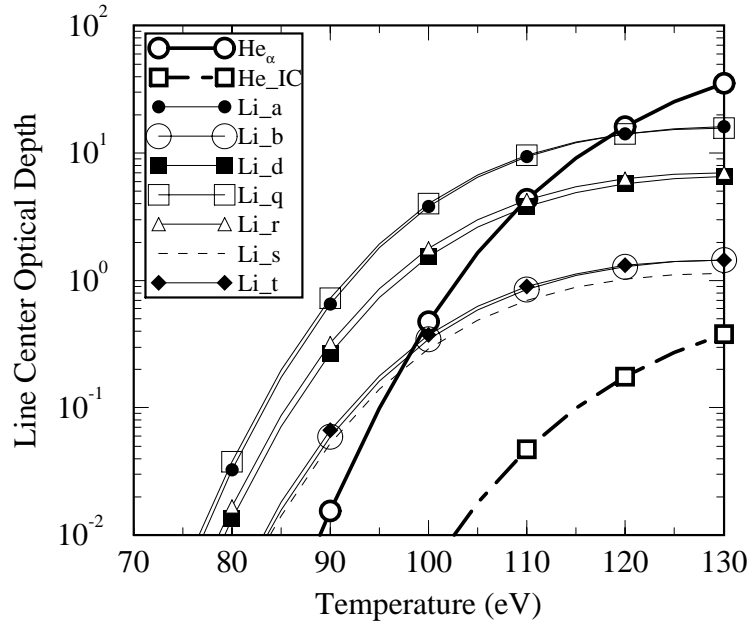
Figure 13.   Temperature-dependent line center optical depths calculated for He-like and Li-like K_α satellite lines of Cl with $n = 3 \times 10^{19}$ ions/cm³. Line transitions correspond to those shown in Figure 2.

direct photoionization from ground states and low-lying levels, are important ionization mechanisms for the plasmas parameters discussed in this paper.

Figures 14 and 15 show the sensitivity of the $\mathrm{He_{IC}}/\mathrm{He_\alpha}$ density diagnostic to opacity effects. Since this ratio has little dependence on the ionization distribution, opacity effects are minimal for the $T = 110$ eV Cl and $T = 45$ eV Al cases shown. This occurs despite the fact that the Cl $\mathrm{He_\alpha}$ line center optical depth is $4 - 5$ at $T = 110$ eV and $n = 3 \times 10^{19}$ ions/cm^3, while the $\mathrm{He_{IC}}$ optical depth is $\ll 1$. The reason the $\mathrm{He_\alpha}$ intensity is not reduced is because the scattering, or "quenching", parameter is low. For these conditions, the scattering parameter is 6×10^{-3}, indicating the plasma is "effectively thin" for this line [23,34,35]. However, at higher densities and/or optical depths, there could be a reduction in the relative strength of the $\mathrm{He_\alpha}$ line. When including the nearby Li(st) intensities with the $\mathrm{He_{IC}}$ line, there is a small, but noticeable change in the intensity ratio.

Additional sets of calculations have been performed to investigate the sensitivity of various line ratios to the characteristics of the ion beam. In one series of calculations, the Li beam voltage was lowered from 10 MeV to 7 MeV, while in another a 5 MeV proton beam was substituted for the Li beam. By lowering the Li beam voltage to 7 MeV, we found the Li/He line ratios to be almost indistinguishable from the 10 MeV results. This suggests that beams with energy spreads (i.e., non-monoenergetic beams) or experimental uncertainties in the beam voltage of several tens of percent should not introduce significant sources of uncertainty in the line ratio diagnostics. Figure 16 compares the Li(dabc)/$\mathrm{He_\alpha}$ ratio for Al irradiated by a 5 MeV proton beam and a 10 MeV Li beam. Also shown is the curve for Li without beam-induced multiple ionization included. Here, it is seen that the proton beam result lies very close to that for the Li beam case which neglects multiple ionization. This can be expected because multiple ionization tends to be relatively unimportant for proton beams, but can become very pronounced as the projectile charge increases [27]. At relatively high temperatures, the predicted line intensity ratios for the proton and Li beam cases become almost identical.

4.   Summary

We have presented results from collisional-radiative equilibrium calculations which describe the temperature and density sensitivity of various Li-like and He-like $\mathrm{K_\alpha}$ line intensity ratios which can be utilized in light ion beam fusion experiments. Results were shown for a range of Al and Cl plasma parameters and Li and proton ion beam parameters relevant to present-day and near-future intense light ion beam experiments. As in the case of higher-temperature laser produced plasmas, the line intensity ratios of the Li-like satellites

25
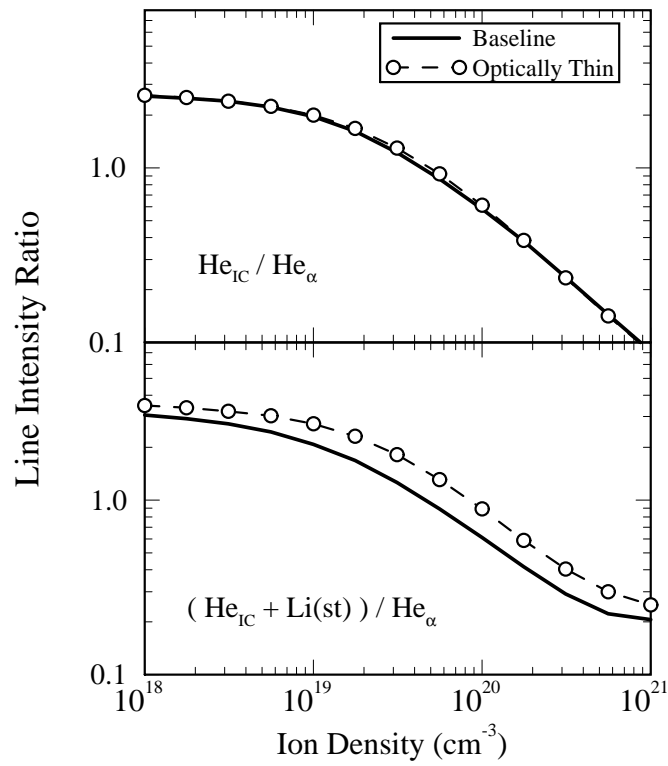
Figure 14. Dependence of density-sensitive line intensity ratios for Cl on opacity effects. The plasma temperature is 110 eV. The Cl ion column density for the baseline case is 1.2×10^{18} ions/cm^2.
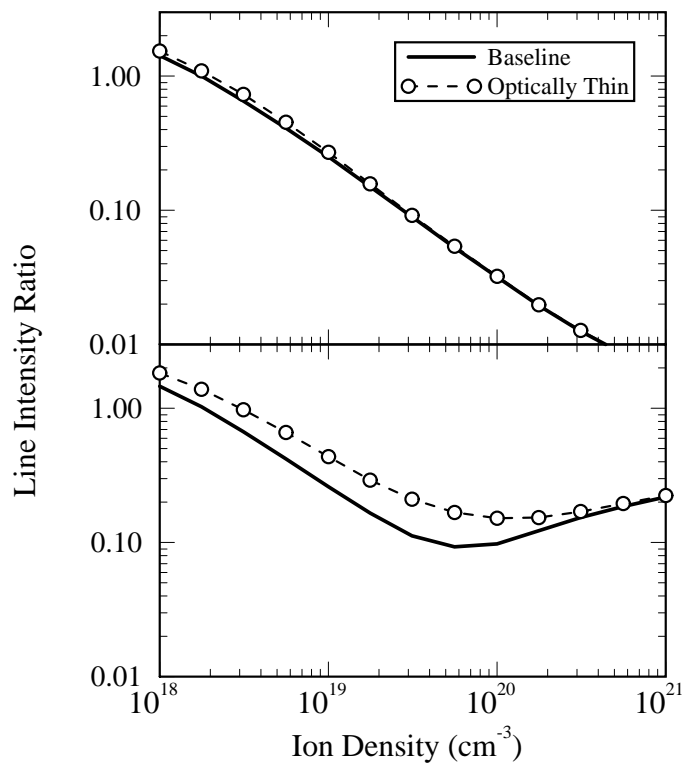
Figure 15.   Dependence of density-sensitive line intensity ratios for Al on opacity effects. The plasma temperature is 45 eV. The Al ion column density for the baseline case is 1.2×10^{18} ions/cm^2.
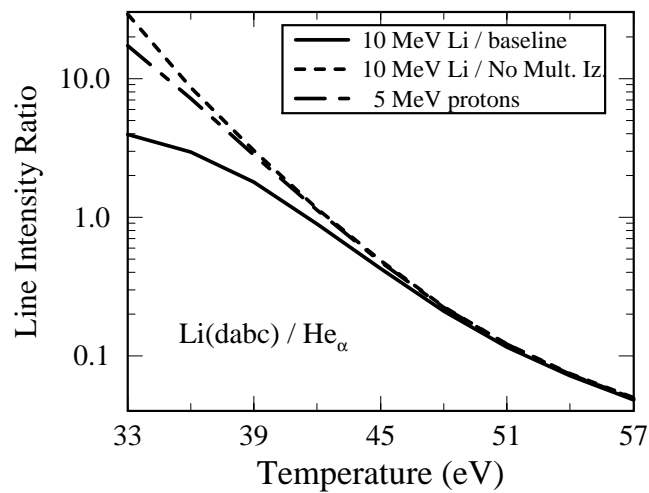
Figure 16.   Comparison of Li(dabc)/He$_\alpha$ line intensity ratio calculated for Cl with $n =$ 3×10^{19} ions/cm^3. The solid curve represents the baseline 10 MeV Li beam case; the dashed curve is similar to the baseline case, but with no multiple ionization included; the dot-dashed curve represents results for a 5 MeV proton beam.

to He_α were found to be good temperature diagnostics, while the He-like intercombination-to-resonance ratio was found to be a good density diagnostic. However, it is important to note that while the upper states of these lines are populated in laser-produced plasmas by dielectronic recombination and electron-impact excitation, in light ion beam-heated plasmas they are populated by ion-impact ionization; i.e., they are populated from lower ionization states. For this reason, these lines are observable and become useful plasma diagnostics at a much lower temperature in ion beam-heated plasmas.

The sensitivity of the calculated K_α line intensity ratios to opacity effects and ion-impact multiple ionization processes were also studied. We find that the density-sensitive $\text{He}_\text{IC}/\text{He}_\alpha$ ratio shows little dependence on either multiple ionization or opacity effects for the plasma parameters studied. The reasons for this are: (1) the different He-like upper states are populated by ion-impact ionization from the same ion; thus, any changes in the ionization distribution of the plasma tend to be cancelled out; and (2) for a large part of the parameter space investigated the He_α line is either optically thin or effectively thin (i.e., emitted photons escape by "scattering"). On the other hand, the temperature-sensitive line ratios investigated exhibit a significant dependence on opacity — i.e., the plasma thickness. This results from the fact that the overall ionization distribution of the plasma changes due to resonant self-absorption and photoionization processes. In addition, it was found that beam-impact multiple ionization can also influence temperature-sensitive Li-like satellite-to-He_α line ratios, although this tended to occur only at relatively low plasma temperatures.

In summary, it is concluded that K_α satellite line ratio diagnostics offer very good prospects for determining plasma conditions in intense light ion beam experiments. Tracer materials could be chosen such that they produce strong Li-like and He-like K_α line emission at the plasma conditions expected in the experiments. It might also be advantageous to use multiple thin tracers of adjacent-Z materials to provide additional constraints on determining target plasma conditions, such as space-dependent information.

Acknowledgements

References

1. De Michelis, C., and Mattioli, M., *Nuclear Fusion* **21**, 677 (1981).

2. Yaakobi, B., Skupsky, S., McCrory, R. L., Hooper, C. F., Deckman, H., Bourke, P., and Soures, J. M., *Phys. Rev. Lett.* **44**, 1072 (1980).

3. Boiko, V. A., Faenov, A. Ya., and Pikuz, S. A., *JQSRT* **19**, 11 (1985).

4. Hammel, B. A., Keane, C. J., Cable, M. D., Kania, D. R., Kilkenny, J. D., Lee, R. W., and Pasha, R., *Phys. Rev. Lett.* **70**, 1263 (1993).

5. Hauer, A., Mitchell, K. B., van-Hulstyen, D. B., Tau, T. H., Linnebur, E. J., Mueller, M. M., Kepple, P. C., and Griem, H. R., *Phys. Rev. Lett.* **45**, 1495 (1980).

6. Apruzese, J. P., Duston, D., and Davis, J., *JQSRT* **36**, 339 (1986).

7. Gabriel, A. H., and Jordan, C., *Nature* **221**, 947 (1969).

8. Duston, D., Rogerson, J. E., Davis, J., and Blaha, M., *Phys. Rev. A* **28**, 2968 (1983).

9. Davis, J., and Jacobs, V. L., *Phys. Rev. A* **12**, 2017 (1975).

10. Hauer, A., Cowan, R. W., Yaakobi, B., Barnouin, O., and Epstein, R., *Phys. Rev. A* **34**, 411 (1986).

11. Chenais-Popovics, C., Fievet, C., Geindre, J. P., Gautheir, J. C., Luc-Koenig, E., Wyart, J. F., Pepin, H., and Chaker, M., *Phys. Rev. A* **40**, 3194 (1989).

12. Perry, T. S., Davidson, S. J., Serduke, F. J. D., Bach, D. R., Smith, C. C., Foster, J. M., Doyas, R. J., Ward, R. A., Iglesias, C. A., Rogers, F. J., Abdallah, Jr., J., Stewart, R. E., Kilkenny, J. D., and Lee, R. W., *Phys. Rev. Lett.* **67**, 3784 (1991).

13. Perry, T. S., Budil, K. S., and Lee, R. W., *JQSRT* **54**, 317 (1995).

14. Springer, P. T., et al., in <u>Atomic Processes in Plasmas</u>, AIP Conference Proceedings 257, E. S. Marmer and J. L. Terry, eds. (Amer. Inst. Phys., New York, 1992).

15. Bailey, J., Carlson, A. L., Chandler, G., Derzon, M. S., Dukart, R. J., Hammel, B. A., Johnson, D. J., Lockner, T. R., Maenchen, J., McGuire, E. J., Mehlhorn, T. A., Nelson, W. E., Ruggles, L. E., Stygar, W. A., and Wenger, D. F., *Lasers Part. Beams* **8**, 555 (1990).

16. Bailey, J. E., Carlson, A. L., Haill, T. A., Johnson, D. J., Lake, P., McGuire, E. J., Mehlhorn, T. A., MacFarlane, J. J., and Wang, P., submitted to *Phys. Rev. E* (1997).

17. MacFarlane, J.J., Wang, P., Bailey, J.E., Mehlhorn, T.A., Dukart, R.J., and Mancini, R.F., *Phys. Rev. E* **47**, 2748 (1993).

18. Meisel, G., Bluhm, H., Hoppe, P., Huttner, R., Rusch, D., Sanger, E., Schon, T., and Singer, J., Forschungszentrum Karlsruhe Report FZKA-5840, Karlsruhe, Germany (1996).

19. Nardi, E., and Zinamon, Z., *J. Appl. Phys.* **52**, 7075 (1981).

20. Chen, H., Soom, B., Yaakobi, B., Uchida, S., and Meyerhofer, D. D., *Phys. Rev. Lett.* **70**, 3431 (1993).

21. Hares, J. D., Kilkenny, J. D., Key, M. H., and Lunney, J. G., *Phys. Rev. Lett.* **42**, 1216 (1979).

22. MacFarlane, J.J., Wang, P., Bailey, J.E., Mehlhorn, T.A., and Dukart, R.J., *Laser Part. Beams* **13**, 231 (1995).

23. Apruzese, J.P., Davis, J., Duston, D., and Whitney, K.G., *J. Quant. Spectrosc. Radiat. Transfer* **23**, 479 (1980).

24. Apruzese, J.P., *J. Quant. Spectrosc. Radiat. Transfer* **34**, 447 (1985).

25. Olson, G.L., and Kunasz, P.B., *J. Quant. Spectrosc. Radiat. Transfer* **38**, 325 (1987).

26. Wang, P., MacFarlane, J.J., and Moses, G.A., *Phys. Rev. E* **48**, 3934 (1993).

27. Watson, R. L., Benka, O., Parthasaradhi, K., Maurer, R. J., and Sanders, J. M., *J. Phys. B* **16**, 835 (1983).

28. Wang, P., MacFarlane, J.J., and Moses, G.A., *Laser Part. Beams* **13**, 191 (1995).

29. Combet Faroux, F., *Journal de Physique*, Coll. C9, Suppl. 12, Tome 48, 199 (1987).

30. Chen, M. H., and Craseman, B., *Phys. Rev. A* **12**, 959 (1975).

31. Duston, D., and Davis, J., *Phys. Rev. A* **21**, 1664 (1980).

32. Vinogradov, A. V., Skobelev, I. Yu., and Yukov, E. A., *Sov. J. Quantum Electron.* **5**, 630 (1975).

33. Kunge, H. J., Gabriel, A. H., and Griem, H. R., *Phys. Rev.* **165**, 276 (1968).

34. Avrett, E. H., and Hummer, D. G., *Mon. Not. R. Astron. Soc.* **130**, 295 (1965).

35. Mihalas, D. 1978, Stellar Atmospheres, Second Edition (Freeman, New York).